

1 **Mineral-melt partition coefficients and the problem of multiple substitution mechanisms:**
2 **insights from the rare earths in forsterite and protoenstatite**

3 Antony D. Burnham* and Hugh St.C. O'Neill

4 Research School of Earth Sciences, Australian National University, Acton ACT 2601, Australia

5 (* corresponding author antony.burnham@anu.edu.au)

6
7 **Abstract**

8 A trace element may substitute into a mineral by more than one substitution mechanism, complicating
9 the thermodynamic description of its partition coefficients. In order to understand this phenomenon
10 better, the mineral/melt partition coefficients for all 14 rare earth elements (REE) plus Y and Sc were
11 measured experimentally for coexisting forsterite and protoenstatite in the system CaO-MgO-
12 $\text{SiO}_2 \pm \text{Al}_2\text{O}_3 \pm \text{TiO}_2$ at 1406 °C and atmospheric pressure. For both phases, the results show these large
13 trivalent cations (REE^{3+}) replace Mg^{2+} on octahedral sites, but with charge-balanced achieved by two
14 different mechanisms: 1) cation vacancies ($2 \text{REE}^{3+} + \text{vacancy} = 3 \text{Mg}^{2+}$); and 2) substitution of Al for
15 Si ($\text{REE}^{3+} + \text{Al}^{3+} = \text{Mg}^{2+} + \text{Si}^{4+}$). The overall REE partition coefficient is the sum of the partition
16 coefficients for each substitution mechanism. Because the stoichiometric control is different for each
17 mechanism, the relative importance of the mechanism varies with melt composition, including the
18 activities of both silica and alumina in the melt ($a_{\text{SiO}_2}^{\text{melt}}$ and $a_{\text{AlO}_{1.5}}^{\text{melt}}$). The coexistence of forsterite and
19 protoenstatite fixes the silica activity, allowing the effect of $a_{\text{AlO}_{1.5}}^{\text{melt}}$ to be separated from that of $a_{\text{SiO}_2}^{\text{melt}}$.
20 The relative importance of the two mechanisms depends strongly on the identity of the REE for
21 forsterite, but not for protoenstatite. The results are used to test the lattice strain model: the two
22 substitution mechanisms in forsterite imply different values for the Young's modulus in the Brice
23 equation, despite the fact that the REE^{3+} cations likely occupy the same crystallographic site in both
24 mechanisms, casting doubt on the physical basis of the lattice strain theory. Comparison with
25 literature data confirms earlier observations that the activity coefficients of REE_2O_3 in silicate melts
26 decrease with increasing SiO_2 content of the melt, but the effect decreases with increasing atomic
27 number, from La to Lu, and is almost negligible for Sc. The influence of melt composition should
28 apply to the mineral/melt REE partition coefficients of all other minerals. Recognising that observed
29 mineral/melt partition coefficients are often the sums of contributions from multiple substitution
30 mechanisms, each with its own dependence on both crystal composition and the stoichiometric
31 control from the melt composition, will improve parameterizations of the mineral/melt partition
32 coefficients of other rock-forming minerals. Partition coefficients for Na, Al, Ca, Ti, and Zr are also
33 reported.

34 **Acknowledgements**

35 We thank Jung-Woo Park for assistance with the LA-ICP-MS analyses, Chris Ballhaus for his
36 editorial supervision and Raúl Fonseca for constructive comments on this and earlier drafts of the
37

38 manuscript. This work was supported by Australian Research Council Laureate Fellowship
39 FL130100066 to HO’N.

40

41 **1. Introduction**

42 Mineral/melt partition coefficients are the enablers of the trace-element approach to understanding the
43 petrogenesis of igneous rocks, through their use in mass-balance equations (e.g., Shaw 2006; Zou,
44 2007). They are defined as the concentration of an element in a mineral phase divided by its
45 concentration in the melt, usually by weight. They depend on the valence state of the element, the
46 compositions of both the mineral and the melt, and temperature and pressure, all of which may be
47 elucidated from the thermodynamic description of the mineral-melt system. Partition coefficients are
48 not, however, thermodynamic entities in themselves, except in special circumstances, as pointed out
49 by Nernst (1890, 1891). Rather, the relationship of a partition coefficient to the thermodynamic
50 description of the mineral-melt system begins with formulating the chemical equilibrium
51 (colloquially, “reaction”) between the relevant component containing the element in the mineral, and
52 the components in the melt that add up to the same composition as the mineral component¹ (e.g.,
53 O’Neill and Eggins 2002). The essence of this concept may be explicated using the well-known
54 example of the partitioning of Ni between olivine and melt, for which the reaction is:



55 The equilibrium constant for this reaction is:

$$K_{Ni}^{ol/melt} = \frac{(a_{\text{Ni}_2\text{SiO}_4}^{ol})^{1/2}}{a_{\text{NiO}}^{melt} (a_{\text{SiO}_2}^{melt})^{1/2}} \quad (2)$$

56 where a_i^{phase} is the activity of component i in a phase. Since a main contribution to an activity is from
57 the configurational entropy of mixing in the phase, which in crystals is related to atomic fractions on
58 individual crystallographic sites, activities are usually evaluated from mole fractions. In this simple
59 case, $a_{\text{Ni}_2\text{SiO}_4}^{ol} = (X_{Ni}^{ol} \gamma_{Ni}^{ol})^2$, where X_{Ni}^{ol} is the mole fraction of Ni in the octahedral sites of the olivine
60 and γ_{Ni}^{ol} is the activity coefficient, which is a function of the major-element composition of the
61 olivine. The exponent of 2 comes from the fact that Ni is considered to mix on two sites per formula

¹ The term “component” has a rigorously defined meaning: it is one of a set of compositional variables that together describe the composition of the phase of interest, whose amount can be varied in that phase independently of the amounts of the other components. The latter consideration means that there exists a well-defined quantity $(\partial G/\partial n_i)_{n_j}$, known as the chemical potential, where G is the Gibbs free energy of the phase, n_i is the amount of component i ($n_i \neq 0$), and n_j are the amounts of the other components in the phase. For example, in the case of Ni partitioning between Mg-rich olivine of general formula $M_2\text{SiO}_4$, where M stands for divalent cations, and silicate melt, the Ni component in olivine is Ni_2SiO_4 , rather than NiO or Ni , because NiO and Ni cannot be varied independently in olivine without violating the constraints of stoichiometry and charge-balance, which are foundation assumptions in the thermodynamics of phase equilibria (e.g., Callen 1985). Point-defect thermodynamics, which describes excursions from these constraints, nevertheless confirms their essential validity in the phase-equilibrium context (e.g., Schmalzried 1995). The activity is intimately related to the chemical potential.

62 unit of olivine, although from a crystallographic perspective, this is not correct: Ni orders on to the
 63 M1 octahedral site of olivine (e.g., Boström 1989). The explanation lies in the payoff between the
 64 loss of configurational entropy because of ordering between sites and the enthalpy and other
 65 contributions gained from the ordering, which nearly cancel out to give the observed relationship
 66 (e.g., Seifert and O'Neill 1987). The mole fraction, X_{Ni}^{ol} , is proportional to the concentration of Ni in
 67 olivine by weight, to an excellent approximation in the trace-element concentration regime: $c_{Ni}^{ol} =$
 68 $k_{Ni}^{ol} X_{Ni}^{ol}$. The proportionality factor, k_{Ni}^{ol} , is, like γ_{Ni}^{ol} , also a function of the major-element composition
 69 of the olivine, so the two are sometimes combined into one term. Similar considerations apply to the
 70 components in the melt, here NiO and SiO₂.

71 The partition coefficient is defined as:

$$D_{Ni}^{ol/melt} = \frac{c_{Ni}^{ol}}{c_{Ni}^{melt}} \quad (3)$$

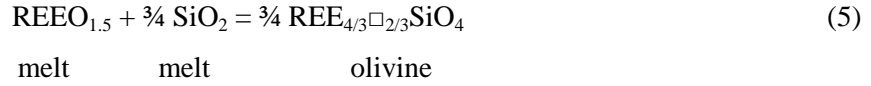
72 where c_M^{phase} is the weight concentration of element M in a phase. Combining these relationships and
 73 rearranging gives:

$$D_{Ni}^{ol/melt} = K_{Ni}^{ol/melt} \cdot \frac{\gamma_{NiO}^{melt} k_{NiO}^{melt}}{\gamma_{Ni}^{ol} k_{Ni}^{ol}} \cdot (a_{SiO_2}^{melt})^{1/2} \quad (4)$$

74 This emphasises that partition coefficients vary not only with the composition of the mineral (here,
 75 through $\gamma_{Ni}^{ol} k_{Ni}^{ol}$), but with melt composition, through two conceptually different and independently
 76 measurable factors, which in this case are $\gamma_{NiO}^{melt} k_{NiO}^{melt}$ and $a_{SiO_2}^{melt}$. Several studies have measured
 77 $\gamma_{NiO}^{melt} k_{NiO}^{melt}$ independently of $D_{Ni}^{ol/melt}$ (e.g. O'Neill and Eggins 2002) and found it to vary by about a
 78 factor of two in melts saturated in olivine at magmatic temperatures and atmospheric pressure. But
 79 quantitatively the more significant variable is $a_{SiO_2}^{melt}$, which may cover one to two orders of magnitude,
 80 depending on temperature, in systems containing olivine and silicate melt (e.g., see Fig. 3 of Zhukova
 81 et al. 2017). This is an example of the “stoichiometric control” on partition coefficients (Takahashi
 82 and Irvine 1981; O'Neill and Eggins 2002).

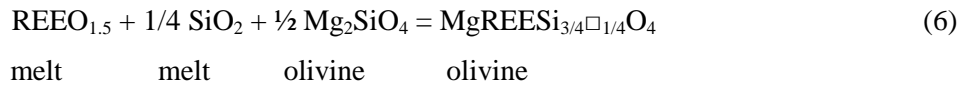
83
 84 Thus the thermodynamic description of element partitioning between mineral and melt is founded on
 85 being able to identify the relevant component in the mineral, and then evaluating the form of its
 86 configurational entropy of mixing. In the example of $D_{Ni}^{ol/melt}$, it is obvious from crystal-chemical
 87 considerations that the relevant component for Ni in olivine is Ni₂SiO₄, and it is unsurprising that the
 88 simple substitution of Ni for Mg (or Fe²⁺) in the olivine structure should give the $a_{Ni_2SiO_4}^{ol} \propto (X_{Ni}^{ol})^2$
 89 relationship. But elsewhere identifying substitution mechanisms and their configurational entropies
 90 may be more difficult, especially where the substituting element requires charge-balancing. Here
 91 again, olivine/melt partitioning can provide an instructive example, this time of the Rare Earth
 92 Elements (REE). The REE form 3+ cations that are too large to substitute for Si in the tetrahedral site
 93 of olivine, and therefore replace Mg, a divalent cation, in octahedral coordination, probably on the M2

94 octahedral site, which favours larger cations like Ca (e.g., Blasse and Bril, 1967). For charge-
 95 balancing this substitution, there are several possibilities. The most often suggested is by octahedral-
 96 site vacancies (Colson et al. 1989; Nielsen et al. 1992; Evans et al. 2008), making the relevant
 97 thermodynamic component $\text{REE}_{4/3}\square_{2/3}\text{SiO}_4$, where the symbol \square stands for a vacancy. (The
 98 component could be written $\text{MgREE}_{2/3}\square_{1/3}\text{SiO}_4$, which in the present context comes to the same thing,
 99 see Evans et al. 2008). The partitioning equilibrium is:



100 which gives the stoichiometric control as $D_{\text{REE}}^{\text{ol/melt}} \propto (a_{\text{SiO}_2}^{\text{melt}})^{3/4}$ (Evans et al. 2008).

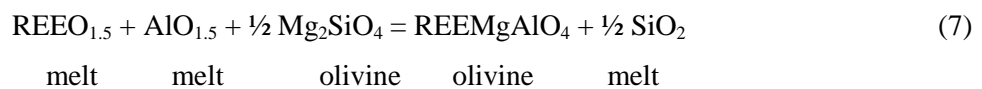
101 A different possibility would be charge-balancing with tetrahedral-site vacancies, which would give
 102 the component as $\text{MgREESi}_{3/4}\square_{1/4}\text{O}_4$. The partitioning equilibrium would then be:



105 and the stoichiometric control would have $D_{\text{REE}}^{\text{ol/melt}} \propto (a_{\text{SiO}_2}^{\text{melt}})^{1/4}$. It may look as though it should be
 106 possible experimentally to distinguish between these alternatives by measuring the dependence of

107 $D_{\text{REE}}^{\text{ol/melt}}$ on $a_{\text{SiO}_2}^{\text{melt}}$, but in practice the relationship is obscured by the dependence of $D_{\text{REE}}^{\text{ol/melt}}$ on
 108 $\gamma_{\text{REEO}_{1.5}}^{\text{melt}}$, the activity coefficient of the $\text{REEO}_{1.5}$ component in the silicate melt, because the latter is a
 109 strong function of the SiO_2 content of the melt (Evans et al. 2008), and therefore also of $a_{\text{SiO}_2}^{\text{melt}}$. That
 110 the substitution mechanism is by charge-balancing by octahedral-site vacancies (Eq. 5) and not
 111 tetrahedral-site vacancies (Eq. 6) is now based on inference from hydroxylation spectroscopy (Berry
 112 et al. 2007), and this assignment will be assumed in the rest of this paper.

113 But even for the relatively simple case of $D_{\text{REE}}^{\text{ol/melt}}$ there are more options, because of charge-
 114 balancing by coupled substitution with other elements. Several authors have proposed charge-
 115 balancing of the REE substitution in olivine by coupled substitution of Al^{3+} replacing Si^{4+} on
 116 tetrahedral sites (Beattie 1994; Taura et al. 1998). This gives the component REEMgAlO_4 , for which
 117 the partitioning equilibrium is:



118 In this case the stoichiometric control predicts $D_{\text{REE}}^{\text{ol/melt}} \propto (a_{\text{SiO}_2}^{\text{melt}})^{-1/2}$, hence this substitution would
 119 be favoured by lower $a_{\text{SiO}_2}^{\text{melt}}$, but is obviously only possible if there is alumina in the system.

120 This example of the partitioning of the REEs between olivine and melt brings another issue into
 121 focus: there is no reason to suppose, *a priori*, that any one substitution mechanism dominates to the
 122 exclusion of all the others. This possibility has been noted by most previous workers, but has not been
 123 quantitatively explored.
 124

125
126 Here we report an experimental study of this problem, in which we investigate how the partitioning of
127 REE between olivine and melt changes as a function of Al_2O_3 in the melt, while holding temperature,
128 pressure and $a_{\text{SiO}_2}^{\text{melt}}$ constant. The buffering of $a_{\text{SiO}_2}^{\text{melt}}$ was achieved with coexisting protoenstatite,
129 $\text{Mg}_2\text{Si}_2\text{O}_6$; serendipitously, this mineral shows the same two substitution mechanisms for REE as
130 forsterite (i.e., the components $\text{REE}_{4/3}\square_{2/3}\text{Si}_2\text{O}_6$ and REEMgSiAlO_6), allowing the same phenomenon
131 to be compared side-by-side in different minerals. The partition coefficients of all 14 REEs plus Y and
132 Sc were determined, to see whether the two mechanisms affect the REE differently, with implications
133 for the use of lattice strain theory in modelling trace element partitioning. We also included a melt
134 composition rich in TiO_2 in order to change melt composition independently of olivine composition
135 and alumina activity. Our aim is to obtain quantitative information on an example of the phenomenon
136 of multiple substitution mechanisms in trace-element partitioning, which will be of heuristic value in
137 refining the way mineral/melt trace-element partition coefficients in general are parameterized. The
138 example of REE partitioning between olivine and melt was chosen for this purpose not only to build
139 on the previous experimental and theoretical work reviewed above, but also because Mg_2SiO_4 -rich
140 forsterite provides a compromise between simplicity of composition and crystal structure, while still
141 having the complexity to exhibit multiple substitution mechanisms.

142

143 **2. Methods**

144 A base composition in the system CaO-MgO-SiO_2 designed to crystallize approximately 15% each of
145 protoenstatite and forsterite was prepared by combining weighed proportions of SiO_2 , MgO , CaCO_3 ,
146 the REE oxides (all REE_2O_3 apart from CeO_2 , Pr_6O_{11} and Tb_4O_7) and Sc_2O_3 under acetone using an
147 agate pestle and mortar. We used a high level of doping in light REE to achieve good precision in the
148 partition coefficients, based on the experience of Evans et al. (2008). Because the REEs are heavy
149 elements, these high levels translate to a sum of mole fractions of the REE oxide components
150 ($\sum \text{XREEO}_{1.5}$) of 0.029 to 0.056, compared to 0.012 to 0.015 in the study of Evans et al. (2008). Thus
151 although large on a weight-percent basis, the doping levels may be considered modest in terms of
152 mole fractions, and are not expected to have a significant effect on the results, as discussed below.
153 The amounts of REE oxides added varied with the incompatibility of the REE, from approximately
154 2% for La and Ce to 0.02 wt% for Sc and some of the heavy REEs, totalling 6.9 wt%. Three further
155 compositions were prepared by adding 2 wt% Al_2O_3 , 5 wt% Al_2O_3 and 5 wt% TiO_2 to the base mix.
156 Three elements, Na, Zr and Y, occur as impurities in the starting chemicals at sufficiently high
157 concentrations to be analysed profitably in the run products, as does Ti in the three compositions
158 nominally free of this element. The prepared powders were affixed to Pt wire loops using
159 polyethylene oxide solution and, after drying, were run simultaneously in a vertical Gero tube furnace
160 at 1406 °C (loaded at 600 °C and heated to the target at 6 °C/min, monitored using a Type B

161 thermocouple) for 20 days under flowing CO₂ ($f_{O_2} = 10^{-3.05}$ bars) before being dropped into water to
162 quench.

163

164 The resulting beads were mounted in epoxy, ground and polished. Electron probe microanalysis
165 (EPMA) of the glass, forsterite and protoenstatite was performed using a Cameca SX-100 electron
166 probe at the Research School of Earth Sciences (Australian National University). The elements
167 analysed, the standards used, analysing crystal and the background positions were Si K α (quartz,
168 TAP, -600, +500), Ti K α (rutile, PET, -500, +600), Al K α (K412 glass, TAP, -500, +500), Mg K α
169 (San Carlos olivine, TAP, -800, +600), Ca K α (K412 glass, PET, -500, +400), La L α (LaPO₄, PET, -
170 400, +400), Ce L α (CePO₄, PET, n/a, +500), Pr L β (PrPO₄, -460, +330), Nd L β (NdPO₄, LLIF, -350,
171 n/a), Sm L β (SmPO₄, LLIF, n/a, +370), Eu L β (EuPO₄, LLIF, -350, +465) and Gd L β (GdPO₄, LLIF,
172 -442, +420). The REE phosphate standards (Jarosewich and Boatner, 1991) were measured using the
173 same analytical routine and the results used to correct the glass analyses. Only La₂O₃, Eu₂O₃ and
174 Gd₂O₃ required a correction of >0.01 %. The REEs were below the limits of detection in the
175 protoenstatite and forsterite; the reason for analysing them in the glasses by EPMA was to provide the
176 correction factors for the other major elements, and to check that analytical totals were near 100%.
177 Precise trace-element analyses of the glass, forsterite and protoenstatite were obtained by laser-
178 ablation inductively-coupled-plasma mass-spectrometry (LA-ICP-MS) using a 193 nm excimer laser
179 in a HelEx ablation cell coupled to an Agilent 7700 quadrupole mass spectrometer. The spot size was
180 28 μm and fluence was 3 – 4 J cm⁻² at a pulse rate of 5 Hz, with counting times 20 s on background
181 and 45 s on glass or crystal. For each experiment, seven spots were taken on the glass and between six
182 and 17 on the crystals. For the crystals, the laser ablated through to glass during the 45 s of the
183 analysis on many occasions. Where this occurred during the first 25 s or so of ablation, the analysis
184 was abandoned, otherwise the contaminated part was excised during data processing. Approximately
185 half the protoenstatite analyses and a quarter of the forsterite were affected. NIST 610 glass was used
186 as the external standard with concentrations of all elements from Jochum et al. (2011), and ²⁹Si was
187 used as the internal standard, referenced to Si concentrations measured by EPMA. The isotopes
188 measured were ²³Na, ²⁷Al, ²⁹Si, ⁴³Ca, ⁴⁵Sc, ⁴⁹Ti, ⁸⁹Y, ⁹⁰Zr, ¹³⁹La, ¹⁴⁰Ce, ¹⁴¹Pr, ¹⁴⁶Nd, ¹⁴⁷Sm, ¹⁵³Eu, ¹⁵⁷Gd,
189 ¹⁵⁹Tb, ¹⁶³Dy, ¹⁶⁵Ho, ¹⁶⁶Er, ¹⁶⁹Tm, ¹⁷²Yb and ¹⁷⁵Lu. The ablation data were reduced using an in-house
190 spreadsheet, which permitted thorough checking of the time-resolved signals to exclude
191 contamination from melt, including melt inclusions, and to eliminate the occasional electronic blip.
192 Following Jenner and O'Neill (2012) we determined the interference of ²⁹Si¹⁶O on ⁴⁵Sc using an in-
193 house San Carlos olivine standard with 2.32±0.02 ppm Sc, and used the SiO⁺/Si⁺ production rate to
194 subtract the interference, approximately 0.5 ppm, from the olivine and glass data. This correction was
195 never larger than 3% relative for the data presented here.

196

197 **3. Results**

198 The experiments quenched to homogeneous glasses with crystals of forsterite and protoenstatite (up to
199 60 μm) as the liquidus phases. The protoenstatite crystals were commonly cracked, which is attributed
200 to the orthorhombic to monoclinic transition during cooling (Kamenetsky et al., 2006). Major-element
201 compositions by EPMA are given in Table 1 and minor and trace elements by LA-ICP-MS are given
202 in Table 2. The analyses for forsterite and protoenstatite are in good agreement with the expected
203 stoichiometries of these phases. A comparison of data for the elements analysed by both EPMA and
204 LA-ICP-MS in the glasses indicates that the LA-ICP-MS values for Mg and Ca were both too low
205 relative to the EPMA data by 13 % on average, with the exception of the high-Ti glass. The EPMA
206 data for Eu are, for unknown reasons, on average about 40% lower than the LA-ICP-MS values. The
207 LA-ICP-MS data are much more precise and were used for calculating the partition coefficients for all
208 elements. Although there may be some systematic errors in absolute values reported due to matrix
209 effects, as indicated by the different ways in which the count rates for different elements change with
210 depth during ablation between the NIST 610 glass and the forsterite, protoenstatite and experimental
211 glasses (e.g., Jenner and O'Neill, 2012), these largely cancel out in the comparisons between REEs,
212 and between the different experiments. Any errors in the reported reference concentrations of
213 elements in the NIST 610 standard cancel out completely when calculating partition coefficients.

214

215 The trace elements studied are all incompatible in protoenstatite and forsterite (Table 3), with
216 protoenstatite/melt partition coefficients ranging from $D_{\text{La}} = 1.6(2) \times 10^{-5}$ in the Al-free composition
217 to $D_{\text{Sc}} = 0.25(1)$ in the most Al-rich composition. Forsterite/melt partition coefficients are mostly
218 within a factor of three of the corresponding protoenstatite/melt partition coefficients, with the
219 exception of Al, Ti and Na, which are more compatible in protoenstatite than in forsterite (Fig. 1). In
220 the base composition, protoenstatite is more accommodating of the light REEs, but forsterite has a
221 slightly higher preference for the heavy REEs and Sc (Fig. 1).

222

223 The relative standard deviations (RSDs) of the trace elements in the glasses are nearly all in the range
224 1 to 3% (Table 2). The results from the crystals are quite different. The RSDs for the undoped
225 elements (Na, Ti, Y and Zr) in the crystals are large because their low concentrations approach the
226 limits of detection. The limit of detection, calculated after Longerich et al. (1996), is different for each
227 analysis but typical values lie in the range 5 - 10 ppm Na, 630 – 710 ppb Ti, 2 – 10 ppb Y, 5 – 15 ppb
228 Zr. Another explanation must be sought where the REEs have high RSDs, as all REEs are well above
229 the limit of quantification. The distinction between the two causes of high RSDs is well illustrated by
230 comparing the RSDs of Y with those of La. In the protoenstatite of the low-Al experiment, the RSD
231 of Y is 23%, but its concentration is only 0.03 ppm, very close to the limit of detection, whereas for
232 La the RSD is 44%, although present at the much healthier concentration of 3.4 ppm. On the other
233 hand, La and Yb have a similar number of counts per time slice in the LA-ICP-MS analyses, La in

234 protoenstatite, with an RSD of ~ 45%, is much more inhomogeneous than Yb, with RSDs of ~ 2%.
235 The effect is much larger in protoenstatite than forsterite. We propose that the elevated standard
236 deviations of the more incompatible REEs in protoenstatite are due to undetected contamination by
237 glass in the ablated volume. This phenomenon is particularly severe for highly incompatible elements,
238 as can be seen by the following thought experiment. Where the mineral analysis includes a mass
239 fraction x of glass, then an apparent partition coefficient D^* results:

$$D^* = \frac{(1-x)c^{xtl} + xc^{melt}}{c^{melt}} \quad (8)$$

240 which simplifies to $D^* = D + x$ for small values of x . Hence, the relative importance of any non-zero
241 value of x is inversely proportional to D . In Fig. 2 we compare partition coefficients for all REE in
242 protoenstatite in the two Al-free compositions. The partition coefficients differ considerably for the
243 light REE (La to Nd) but are more closely correlated for the heavy REE, conforming to the pattern we
244 would expect for melt contamination. Although it is not possible to know *a priori* how the partition
245 coefficients will vary due to the presence of TiO_2 in one of the experiments, a value of $x = 0.00003$
246 (i.e., 30 parts per million) results in a straight-line correlation between $(D^* - x)$ for the low-Al series
247 and D for the Al-series. Such small volumes would not be observable optically, and if diffusely
248 distributed would not be evident in the time-resolved signal of the ICP-MS. The forsterite analyses
249 also show an increase of RSD with incompatibility, but more muted, and we have no reason to
250 suppose that in forsterite the effect is not simply that expected from the counting statistics.
251 Protoenstatite may be more susceptible to contamination if the cracks in the crystals, which we
252 attribute to the volume change caused by the inversion to the monoclinic pyroxene during quenching,
253 provide pathways for insertion of melt, although we avoided visible cracks during analysis. As Fig. 2
254 shows, the putative contamination becomes insignificant for REE heavier than Nd.

255

256 **4. Discussion**

257 *4.1 REE oxidation states*

258 Two of the REE (Ce and Eu) are known to exist in oxidation states other than 3+ in geological
259 materials, but in these experiments their partition coefficients are not noticeably anomalous relative to
260 the neighbouring elements (La and Pr, and Sm and Gd, respectively). This is in qualitative agreement
261 with the small amounts of Eu^{2+} and Ce^{4+} expected under the experimental conditions: we calculate
262 that only 2 to 4% % of the Eu in the melt was Eu^{2+} (Burnham et al., 2015), while 4 to 5% of the Ce
263 was Ce^{4+} (Burnham and Berry, 2014). The optical basicities of the REE needed for these calculations
264 were taken from Duffy (2005). The partitioning data of Leitzke et al. (2017) indicate that the presence
265 of Eu^{2+} should give rise to a negative Eu anomaly in the partition coefficients, which is not observed
266 in the present study; similarly, neither Eu nor Ce anomalies occurred in the forsterite/melt partitioning
267 experiments of Evans et al. (2008), which were performed in air. Hence all Ce and Eu were
268 considered to be trivalent in the following discussion.

269

270 4.2 Major-element relations

271 The coexistence of nearly pure forsterite (fo) and protoenstatite (prEn) fixes the activities of both
272 MgO and SiO₂ each at nearly the same values in all four compositions. In detail, the deviations from
273 the pure components Mg₂SiO₄ and Mg₂Si₂O₆ with the minor substitutions of Ca and Al almost cancel
274 out as Al increases and Ca decreases in the base, lo-Ti and hi-Ti compositions, making this an
275 excellent approximation. Since $a_i^{\text{melt}} = X_i^{\text{melt}} \gamma_i^{\text{melt}}$, where a_i^{melt} are activities, X_i^{melt} are mole fractions,
276 and γ_i^{melt} are activity coefficients, the fact that $X_{\text{SiO}_2}^{\text{melt}}$ and $X_{\text{MgO}}^{\text{melt}}$ hardly change when Al₂O₃ is added to
277 the base composition means that $\gamma_{\text{SiO}_2}^{\text{melt}}$ and $\gamma_{\text{MgO}}^{\text{melt}}$ stay almost constant, because $a_{\text{SiO}_2}^{\text{melt}}$ and $a_{\text{MgO}}^{\text{melt}}$ are
278 constant on the fo+prEn cotectic. By contrast, adding TiO₂ causes a marked decrease of $X_{\text{SiO}_2}^{\text{melt}}$, hence
279 an increase in $\gamma_{\text{SiO}_2}^{\text{melt}}$. These major-element systematics are qualitatively similar to those noted by
280 Kushiro (1975) from the loci of the fo+prEn cotectics in CaO-free ternary MgO-SiO₂-XO_n systems,
281 where XO_n is a third major-element oxide component. An advantage of the CaO-MgO-SiO₂-XO_n
282 systems is that the cotectic may be followed along paths of increasing XO_n isothermally. Although an
283 increase of about 20% in $D_{\text{Ca}}^{\text{prEn/melt}}$ and $D_{\text{Ca}}^{\text{fo/melt}}$ may be resolved with increasing $X_{\text{CaO}}^{\text{melt}}$ (Fig. 3), and
284 hence a decrease by this amount in $\gamma_{\text{CaO}}^{\text{melt}}$, the magnitude is relatively small, and as a first
285 approximation we propose to treat it as constant. For Al, it is the square root of its concentration in
286 both protoenstatite and forsterite that varies with $X_{\text{AlO}_{1.5}}^{\text{melt}}$, which is thought to be due to short-range
287 order between octahedral and tetrahedral Al, rather than any change of $\gamma_{\text{AlO}_{1.5}}^{\text{melt}}$ (Evans et al., 2008;
288 Burnham and O'Neill, 2016). With $\gamma_{\text{SiO}_2}^{\text{melt}}$, $\gamma_{\text{MgO}}^{\text{melt}}$, $\gamma_{\text{CaO}}^{\text{melt}}$ and probably $\gamma_{\text{AlO}_{1.5}}^{\text{melt}}$ all close to constant in the
289 compositions studied, it seems plausible from the Gibbs-Duhem relation ($\sum X_i d(\ln \gamma_i) = 0$) for the
290 activity coefficients of the other components, $\gamma_{\text{REEO}_{1.5}}^{\text{melt}}$, etc., also to be constant over this range of
291 melt compositions (quasi-ideal mixing). The approximation of constant activity coefficients in melts
292 on the fo+prEn cotectic will be invoked in the modelling below.

293

294 4.3 Henry's Law

295 Henry's Law describes the situation where the activity coefficient of a component in a phase does not
296 vary with the concentration of that component in that phase. It does not address the change of activity
297 coefficients with other components, as discussed in the previous section. In the context of trace-
298 element partitioning studies, an element i is said to follow Henry's Law if D_i is independent of the
299 concentration of i in the system, implying that Henry's Law is followed in both phases.

300 In previous work, McKay (1986) showed in his study of olivine/melt partitioning of Sm, Gd and Yb,
301 that Henry's Law was followed to concentrations of 5 wt% of individual REE₂O₃ in the melt. In the
302 case of Yb, the level of doping in the olivines in the experiments of McKay (1986) extended up to 800

303 ppm, which compares with a maximum concentration in olivine for any REE in this study of 18 ppm
304 (for Er), see Table 2. Total REE, Y and Sc concentrations do not exceed 100 ppm. This constancy of
305 partition coefficients independent of concentration was assumed in subsequent parameterizations of
306 experimental data that have combined results from studies that used different composition ranges
307 (e.g., Beattie 1994; Sun and Liang 2013). The present results contain several observations that
308 reinforce this finding. Despite the greater uncertainties caused by its lower concentrations, the
309 partition coefficients for Y for both protoenstatite/melt and forsterite/melt fall consistently between
310 those of Ho and Er, and closer to the former, as expected from the close coherence of these elements
311 in most rocks (Pack et al., 2007). The Y concentrations are approximately 150 times less than those of
312 Ho and 500 times less than those of Er in three of the four compositions (for unknown reason, Y
313 levels are about 5 times higher in the phases in the base composition experiment), showing that there
314 is no significant deviation from Henry's law over this range, which may allay fears about the high
315 doping levels of the experiments. The same conclusion may be drawn from noting that the values of
316 the partition coefficients of REEs with adjacent atomic numbers but different doping levels fall on the
317 same smooth curves of $D_{\text{REE}}^{\text{fo/melt}}$ or $D_{\text{REE}}^{\text{prEn/melt}}$ versus ionic radii (see Section 4.7 below); this is best
318 exemplified by the adjacent pair Er ($Z = 68$) and Tm ($Z=69$), whose doping levels differ in the
319 experimental melts by an order of magnitude. These smooth curves for $D_{\text{REE}}^{\text{fo/melt}}$ versus atomic number
320 are effectively identical in shape to those of Di Stefano et al. (2018) for Fe-containing olivine,
321 allowing for the differences in the olivine composition and the major-element melt composition,
322 despite the ratios of REE concentrations differing by factors from 10^{-3} to 20 between the two sets of
323 experiments, as shown in Fig. 4. The present data are also in agreement with the results of Evans et al.
324 (2008; see Section 4.3 below for a more detailed comparison), in which the REE concentrations in the
325 melt totalled $\sim 4\%$ REE₂O₃. Taken together, all this evidence suggests that olivine/melt partition
326 coefficients are independent of concentration from a few ppm to over 10% REE₂O₃ in the melt. This
327 observation joins an increasing body of evidence showing that high concentrations of incompatible
328 elements in silicate melts do not by themselves lead to significant deviations from Henry's Law. For
329 example, Schoneveld and O'Neill (2019) report partition coefficients for the REE between anorthite
330 and melt that do not vary over an order of magnitude, with total doping of $\sum \text{REE}_2\text{O}_3$ from 2 to 11
331 wt%. Jollands et al. (2014) found constant partition coefficients of Zr and Hf into forsterite from a few
332 parts per million up to zircon/hafnon saturation, at which the Zr or Hf concentration in the melt
333 approaches 10 wt%. In the same vein, $D_{\text{Ti}}^{\text{prEn/melt}}$ (the partition coefficient for Ti between protoenstatite
334 and melt) in the nominally Ti-free base composition is only $\sim 25\%$ higher than that in the high-Ti
335 composition with 9 wt% TiO₂ in the melt, despite the ratio of concentrations being nearly 10^3 ; similar
336 constancy of $D_{\text{Ti}}^{\text{fo/melt}}$ was observed by Leitzke et al. (2016) with TiO₂ in the melt ranging from 1 to 18
337 %. Another test of Henry's law for protoenstatite is that the experimental values of D_{Ti} , D_{Sc} and D_{Y}
338 are in good agreement with the values for natural samples, despite large differences in concentration,

339 as are those for D_{Ca} (Yurimoto and Sueno, 1987). The concentrations of the REEs, Y and Sc in the
 340 protoenstatites of this study are similar to those in the coexisting forsterites (Table 2).

341

342 4.4 Two substitution mechanisms for REE in forsterite in CMAS

343 The results from the base composition support the inference of Evans et al. (2008) and previous
 344 workers (e.g., Colson et al. 1986; Nielsen et al. 1992; Beattie 1994) that the REE can substitute into
 345 olivine by a vacancy-coupled mechanism (Eq. 5). With the addition of alumina, values of $D_{REE}^{fo/melt}$
 346 increase linearly with $X_{AlO_{1.5}}^{melt}$ (Fig. 5). Under our assumption that $\gamma_{AlO_{1.5}}^{melt}$ is constant, this means that
 347 $D_{REE}^{fo/melt}$ is linearly dependent on $a_{AlO_{1.5}}^{melt}$. Hypothetically, this might be ascribed to an increase in
 348 $\gamma_{REEO_{1.5}}^{melt}$ with added alumina, but this would change $D_{REE}^{fo/melt}$ and $D_{REE}^{prEn/melt}$ identically for all REE,
 349 which is not the case: another advantage of these doubly-saturated experiments.

350

351 Instead, our preferred explanation is as follows. The equilibrium constant for reaction (5) and (7) are:

$$K_{(fo, vac)} = \frac{(a_{REE_{4/3}SiO_4}^{fo})^{3/4}}{a_{REEO_{1.5}}^{melt}(a_{SiO_2}^{melt})^{3/4}} = \exp\{-\Delta G_{(fo, vac)}^{\circ}/RT\} \quad (9)$$

352 and

$$K_{(fo, Al)} = \frac{a_{REEMgAlO_4}^{fo}(a_{SiO_2}^{melt})^{1/2}}{a_{REEO_{1.5}}^{melt}a_{AlO_{1.5}}^{melt}} = \exp\{-\Delta G_{(fo, Al)}^{\circ}/RT\} \quad (10)$$

353 From which, using the assumptions about configurational entropy outlined in Appendix A, the
 354 partition coefficients are:

$$D_{REE(vac)}^{fo/melt} = K_{(fo, vac)} (\gamma_{REEO_{1.5}}^{melt} / \gamma_{REE_{4/3}SiO_4}^{fo}) (a_{SiO_2}^{melt})^{3/4} \quad (11)$$

355 and

$$D_{REE(Al)}^{fo/melt} = K_{(fo, Al)} (\gamma_{REEO_{1.5}}^{melt} / \gamma_{REEMgAlO_4}^{fo}) a_{AlO_{1.5}}^{melt} (a_{SiO_2}^{melt})^{-1/2} \quad (12)$$

356

357 From $C_{REE}^{fo} = C_{REE(vac)}^{fo} + C_{REE(Al)}^{fo}$, it follows that $D_{REE}^{fo/melt} = D_{REE(vac)}^{fo/melt} + D_{REE(Al)}^{fo/melt}$. Then, by
 358 combining Eqns. 11 and 12:

$$D_{REE}^{fo/melt} = \gamma_{REEO_{1.5}}^{melt} [K'_{(fo, vac)} (a_{SiO_2}^{melt})^{3/4} + K'_{(fo, Al)} (X_{AlO_{1.5}}^{melt} \gamma_{AlO_{1.5}}^{melt}) (a_{SiO_2}^{melt})^{-1/2}] \quad (13)$$

359 Here we have changed the standard state of $REE_{4/3}SiO_4$ and $REEMgAlO_4$ from the pure endmember
 360 component to that of the component at unit concentration but exhibiting infinite-dilution behaviour,
 361 by putting $K'_{(fo, vac)} = K_{(fo, vac)} / \gamma_{REE_{4/3}SiO_4}^{fo}$ and $K'_{(fo, Al)} = K_{(fo, Al)} / \gamma_{REEMgAlO_4}^{fo}$. The change of standard
 362 state is conducive to clarity because the dependences of $\gamma_{REE_{4/3}SiO_4}^{fo}$ or $\gamma_{REEMgAlO_4}^{fo}$ on the identity of the
 363 REE cannot be separated from those of $K_{(fo, vac)}$ or $K_{(fo, Al)}$ without further information of a kind
 364 beyond the reach of this study (e.g., from calorimetry).

365

366 In the present experiments, $a_{\text{SiO}_2}^{\text{melt}}$ is constant (fixed by the coexistence of fo and prEn), and, as
367 discussed previously, we propose that values of $\gamma_{\text{REEO}_{1.5}}^{\text{melt}}$ and are also constant along the fo+prEn
368 cotectic as the alumina content increases. With this latter assumption, Eq. 12 predicts that a plot of
369 $D_{\text{REE}}^{\text{fo/melt}}$ against $X_{\text{AlO}_{1.5}}^{\text{melt}}$ should yield a straight line, as observed. The intercept is $D_{\text{REE(vac)}}^{\text{fo/melt}}$ (which is
370 given by $\gamma_{\text{REEO}_{1.5}}^{\text{melt}} K^{(fo, vac)} (a_{\text{SiO}_2}^{\text{melt}})^{3/4}$, see Eq. 11), and the slope is $[\gamma_{\text{REEO}_{1.5}}^{\text{melt}} K^{(fo, Al)} \gamma_{\text{AlO}_{1.5}}^{\text{melt}} (a_{\text{SiO}_2}^{\text{melt}})^{-1/2}]$.
371 For the lightest REE (La and Ce), the line is horizontal, hence $D_{\text{REE(Al)}}^{\text{fo/melt}}$ cannot be distinguished from
372 zero, but a non-zero slope is resolvable for the heavy REE, and the slope is even larger for Sc (Fig. 5).
373 Equation 12 shows that the linear relationship between $D_{\text{REE}}^{\text{fo/melt}}$ and $X_{\text{AlO}_{1.5}}^{\text{melt}}$ would not have been so
374 apparent without $a_{\text{SiO}_2}^{\text{melt}}$ being kept constant. The complications expected from not fixing $a_{\text{SiO}_2}^{\text{melt}}$ extend
375 beyond the effects explicit from the $a_{\text{SiO}_2}^{\text{melt}}$ terms in Eq. 12, because $\gamma_{\text{REEO}_{1.5}}^{\text{melt}}$ also varies strongly with
376 $a_{\text{SiO}_2}^{\text{melt}}$, as will be shown in the next section, where we discuss the results of Evans et al. (2008) in the
377 light of the new results presented here. Our thermodynamic analysis makes a general theoretical point:
378 there are pitfalls to inferring the stoichiometry of the of a trace-element substitution from correlations
379 with major elements.

380

381 Values of $D_{\text{REE(vac)}}^{\text{fo/melt}}$ and of $D_{\text{REE(Al)}}^{\text{fo/melt}}$ extrapolated to $X_{\text{AlO}_{1.5}}^{\text{melt}} = 0.15$ for all REE from least-squares
382 fitting of the data are shown in Fig. 6 as a function of ionic radius in 6-fold coordination (our revised
383 values; Table 3); the value of $X_{\text{AlO}_{1.5}}^{\text{melt}} = 0.15$ was chosen for illustrative purposes because this is
384 typical of basaltic melt compositions. The relative importance of the Al-substitution mechanism
385 increases smoothly with decreasing ionic radius, being negligible for the light REE, but for Sc, $D_{\text{Sc(Al)}}^{\text{fo/melt}}$
386 becomes comparable to $D_{\text{Sc(vac)}}^{\text{fo/melt}}$.

387

388 *4.5 Activity coefficients of REEO_{1.5} in silicate melts: re-evaluating the results of Evans et al. (2008)*
389 Distinguishing and separating out the two substitution mechanisms allows the cause of the variation
390 of $D_{\text{REE}}^{\text{fo/melt}}$ with composition observed by Evans et al. (2008) to be reassessed, and the changes in
391 $\gamma_{\text{REEO}_{1.5}}^{\text{melt}}$ for the different REE to be quantified more exactly. The results of the present study (which,
392 unlike the former study, is saturated in forsterite and protoenstatite and hence has equal silica
393 activities for all four compositions) allow us to disambiguate the effect of the Al-substitution in the
394 forsterite from that of changes in $\gamma_{\text{REEO}_{1.5}}^{\text{melt}}$, due, for example, to REEO_{1.5}-SiO₂ interactions. To re-
395 evaluate the data of Evans et al. (2008), which did not fix $a_{\text{SiO}_2}^{\text{melt}}$, we applied a correction for the
396 expected dependence of $D_{\text{REE}}^{\text{fo/melt}}$ on this variable by normalising to $\gamma_{\text{REEO}_{1.5}}^{\text{melt, f+p}}$, the activity coefficients of
397 REEO_{1.5} in a melt on the forsterite + protoenstatite cotectic (Reaction 1 and Eq. 2; for details see

398 Appendix B). Values of $\gamma_{\text{REEO}_{1.5}}^{\text{melt}}/\gamma_{\text{REEO}_{1.5}}^{\text{melt, f+p}}$ calculated from the results of Evans et al (2008) show an
 399 exponentially shaped decrease with $X_{\text{SiO}_2}^{\text{melt}}$, which becomes less pronounced from La through to Lu,
 400 extrapolating to hardly any change in $\gamma_{\text{ScO}_{1.5}}^{\text{melt}}/\gamma_{\text{ScO}_{1.5}}^{\text{melt, f+p}}$ (Fig. 8). Part of the scatter around these trends
 401 was found to be correlated with $X_{\text{CaO}}^{\text{melt}}$, hence the data were parameterized with an extra term in this
 402 variable that vanished for the fo+prEn compositions (for internal consistency), to give:

$$\ln (\gamma_{\text{REEO}_{1.5}}^{\text{melt}}/\gamma_{\text{REEO}_{1.5}}^{\text{melt, f+p}}) = (X_{\text{SiO}_2}^{\text{melt}} - 0.52) (23.7 - 22.5r_{\text{REE}}^{\text{VIII}} - 52.4 X_{\text{CaO}}^{\text{melt}}) \quad (14)$$

403
 404 where $r_{\text{REE}}^{\text{VIII}}$ is the ionic radius in Å of the REE³⁺ cation in 8-fold coordination from Shannon (1976).
 405 The composition DFA-a from Evans et al. (2008), which was noted to be anomalous in that study,
 406 could not be well fitted, and was not used in the final parameterization. The problem is mainly with
 407 the well-determined heavy REE and Sc, so it is unlikely to be an analytical mishap, rather a failure of
 408 the model. The data for two elements were omitted from this treatment: Y, which was imprecisely
 409 determined, and Gd, for which we noticed a small but systematic discrepancy in the values of Evans
 410 et al., possibly due to an interference of ¹⁴¹Pr¹⁶O on ¹⁵⁷Gd, as the Gd/Pr ratio used in those
 411 experiments was only 0.03, versus 0.4 in this study. For the fitted data (12 compositions and 11
 412 elements including Sc) the standard deviation implied from the fit is 10% relative.

413
 414 In summary, the activity coefficients of the REEO_{1.5} components in silicate melts change with melt
 415 composition, especially with silica content, $X_{\text{SiO}_2}^{\text{melt}}$ (as distinct from silica activity, a_{SiO_2} , which affects
 416 partitioning separately via the stoichiometric control $\text{REEO}_{1.5} + \frac{3}{4} \text{SiO}_2 = \frac{3}{4} \text{REE}_{4/3}\square_{2/3}\text{SiO}_4$). The
 417 decrease of $\gamma_{\text{REEO}_{1.5}}^{\text{melt}}$ with increasing silica is largest for La, being approximately a factor of three over
 418 the range of melt compositions studied by Evans et al. (2008), and becomes less pronounced with
 419 increasing atomic number of the REE (or decreasing ionic radius). It is almost negligible for Sc.
 420 These conclusions are robust against the assumptions and approximations used in the above
 421 discussion, which affect all the REE in the same way, but the details of the compositional dependence
 422 implied in our parameterization of $\gamma_{\text{REEO}_{1.5}}^{\text{melt}}/\gamma_{\text{REEO}_{1.5}}^{\text{melt, f+p}}$ (Eq. 14) is less certain, because it is not
 423 completely insensitive to these assumptions and approximations. We also emphasise that the
 424 parameterization only addresses the small range of melt compositions in CMAS that are in
 425 equilibrium with forsterite at 1400°C and atmospheric pressure. It is offered as a counter to the default
 426 assumption that is sometimes invoked in applying lattice strain theory, that variations in $\gamma_{\text{REEO}_{1.5}}^{\text{melt}}$ with
 427 melt composition are negligible. We envisage that Eq. 14 could be used to estimate the magnitude of
 428 likely variations in $\gamma_{\text{REEO}_{1.5}}^{\text{melt}}$ in a given context, to see if they are significant against other uncertainties
 429 and approximations.

430

431 4.6 Comparison of $D_{\text{REE}}^{\text{prEn/melt}}$ with $D_{\text{REE}}^{\text{fo/melt}}$

432 The relationship of $D_{\text{REE}}^{\text{prEn/melt}}$ with $X_{\text{AlO}_{1.5}}^{\text{melt}}$ (e.g., Fig. 8) shows that the REE^{3+} cations substitute into
433 protoenstatite in the CMAS system by the same two mechanisms as in forsterite: that is, vacancy-
434 coupled ($\text{MgREE}_{2/3}\square_{1/3}\text{Si}_2\text{O}_6$), and charge-balanced by Al (MgREEAlSiO_6). The stoichiometric
435 controls should be the same, and the relationship between the activities of these two components and
436 REE concentrations ($c_{\text{REE}}^{\text{prEn}}$) are also likely similar. Although the substitution of Al^{3+} for Si^{4+} occurs
437 over two equivalent tetrahedral sites per formula unit, the relationship between $c_{\text{Al}}^{\text{prEn}}$ and $X_{\text{AlO}_{1.5}}^{\text{melt}}$
438 shows that tetrahedral and octahedral Al are also short-range ordered, as in forsterite (Evans et al.
439 2008).

440

441 There are some salient differences, however (Fig. 6). Whereas the two mechanisms are of subequal
442 importance in forsterite over basaltic ranges of alumina contents, with the vacancy mechanism
443 slightly dominant, in protoenstatite the vacancy mechanism would not be resolvable in melt
444 compositions with natural levels of alumina. Moreover, the slopes of $D_{\text{REE(vac)}}^{\text{fo/melt}}$ and $D_{\text{REE(Al)}}^{\text{fo/melt}}$ vs. $r_{\text{REE}}^{\text{VIII}}$
445 are different, but the slopes of $D_{\text{REE(vac)}}^{\text{prEn/melt}}$ and $D_{\text{REE(Al)}}^{\text{prEn/melt}}$ vs. $r_{\text{REE}}^{\text{VIII}}$ are about the same.

446

447 Zr also becomes more compatible in protoenstatite with increasing $X_{\text{AlO}_{1.5}}^{\text{melt}}$ (Fig. 8), implying
448 substitution as $\text{ZrMgAl}_2\text{O}_6$. A similar increase in the compatibility of Zr in forsterite with increasing
449 $X_{\text{AlO}_{1.5}}^{\text{melt}}$ (Fig. 9) suggests the component $\text{Mg}_{1/2}\square_{1/2}\text{ZrAlO}_4$ or perhaps $\text{Zr}_{5/4}\square_{3/4}\text{AlO}_4$, in addition to the
450 $\text{Zr}\square\text{SiO}_4$ component already identified in Al-free systems (Jollands et al., 2014). The former seems
451 more likely, because it allows the substitution of Al^{3+} for Si^{4+} in the tetrahedral site to lower the
452 octahedral-site vacancy concentration needed for charge-balancing more effectively, resulting in a
453 more even distribution of positive charge over the volume of the crystal lattice in the neighbourhood
454 of the Zr^{4+} impurity.

455

456 4.7 The effect of Ti

457 Since the hi-Ti and base composition experiments are at the same activity of silica, and neither
458 contain Al, the ratios of $D_{\text{REE}}^{\text{fo/melt}}$ and $D_{\text{REE}}^{\text{prEn/melt}}$ between these two compositions (i.e., $[D_{\text{REE}}^{\text{fo/melt}}]_{\text{hi-Ti}}$
459 $/[D_{\text{REE}}^{\text{fo/melt}}]_{\text{base}}$ and $[D_{\text{REE}}^{\text{prEn/melt}}]_{\text{hi-Ti}}/[D_{\text{REE}}^{\text{prEn/melt}}]_{\text{base}}$) should both be equal to the ratio of activity
460 coefficients in the melt, $[\gamma_{\text{REEO}_{1.5}}^{\text{melt, hi-Ti}}/\gamma_{\text{REEO}_{1.5}}^{\text{melt, base}}]$. The two ratios are indeed close to each other, if we
461 allow for probable glass contamination of the light REE determinations of $D_{\text{REE}}^{\text{prEn/melt}}$ as discussed
462 above, but in detail $[D_{\text{REE}}^{\text{prEn/melt}}]_{\text{hi-Ti}}/[D_{\text{REE}}^{\text{prEn/melt}}]_{\text{base}}$ is consistently about 10% higher than $[D_{\text{REE}}^{\text{fo/melt}}]_{\text{hi-Ti}}$
463 $/[D_{\text{REE}}^{\text{fo/melt}}]_{\text{base}}$. The Ti content of the protoenstatite, although considerably greater than that of the
464 forsterite, is equivalent to a mole fraction of only 0.005 of the $\text{Mg}_2\text{Ti}_2\text{O}_6$ component, which hardly

465 seems sufficient to change $[D_{\text{REE}}^{\text{prEn/melt}}]_{\text{hi-Ti}}/[D_{\text{REE}}^{\text{prEn/melt}}]_{\text{base}}$ by as much as 10%. No explanation is at
466 present apparent.

467

468 The observed decrease in $\gamma_{\text{REEO}_{1.5}}^{\text{melt}}$ with added TiO_2 is opposite to that indicated by Eq. 14, if the effect
469 of adding TiO_2 was simply to lower $X_{\text{SiO}_2}^{\text{melt}}$ by dilution. For example, for La, $\gamma_{\text{LaO}_{1.5}}^{\text{melt, hi-Ti}}/\gamma_{\text{LaO}_{1.5}}^{\text{melt, base}}$ is
470 0.82, whereas Eq. 14 would predict $\gamma_{\text{LaO}_{1.5}}^{\text{melt, hi-Ti}}/\gamma_{\text{LaO}_{1.5}}^{\text{melt, base}} = 1.36$. The effect decreases with decreasing
471 ionic radius, and is insignificant for Sc. The qualitative conclusion is that there are significant
472 interactions between the light REE^{3+} cations and Ti^{4+} in silicate melts, at least for melts with high
473 TiO_2 .

474

475 **5. Comparison with previous work**

476 *5.1 Identifying substitution mechanisms*

477 Olivine is not a major repository of REEs, but its relatively simplicity of composition and
478 stoichiometry gives it theoretical interest, which may explain why the partitioning of the REE
479 between olivine and melt has been the object not only of many experimental studies, but also of
480 computational simulations (Purton et al. 1997; Zhang and Wright 2005). While some studies have
481 debated the substitution mechanism, others focussed on the empirical results only, without discussing
482 the mechanisms. Such studies will not be considered further.

483

484 Of the experimental studies that have discussed substitution mechanisms, Nielsen et al. (1992)
485 concluded that the REE^{3+} substituted by vacancy-coupling only, based on the lack of correlation
486 between $D_{\text{REE}}^{\text{ol/melt}}$ and $X_{\text{AlO}_{1.5}}^{\text{melt}}$, as did Grant and Wood (2010) for Sc partitioning, from the lack of
487 correlation between $D_{\text{Sc}}^{\text{ol/melt}}$ and $X_{\text{AlO}_{1.5}}^{\text{melt}}$. Evans et al. (2008) argued that the vacancy mechanism was
488 predominant with only a “minor proportion” of REEMgAlO_4 . The conclusions of Evans et al. (2008)
489 were compromised by the fact that although T and P were kept constant between all samples in these
490 experiments, $a_{\text{SiO}_2}^{\text{melt}}$ was not, causing increasing $X_{\text{AlO}_{1.5}}^{\text{melt}}$ to be correlated with decreasing $X_{\text{SiO}_2}^{\text{melt}}$, hence
491 also decreasing $a_{\text{SiO}_2}^{\text{melt}}$. We can now see from the results of this study that resolving the effect of
492 alumina is only possible when $a_{\text{SiO}_2}^{\text{melt}}$ is kept constant.

493

494 Beattie (1994) favoured REEMgAlO_4 on statistical thermodynamic grounds. Observing that the
495 values of $D_{\text{REE}}^{\text{fo/melt}}$ followed Henry’s Law, he reasoned that this could be best explained if REE^{3+} were
496 charge-balanced by tetrahedral Al with short-range order, such that $a_{\text{REEMgAlO}_4}^{\text{fo}} \propto c_{\text{REE}}^{\text{fo}}$. While we agree
497 with this latter assignment (see Eqns. 7, 10, 12), our results show that his next assumption, that the
498 vacancies in the $\text{REE}_{4/3}\square_{2/3}\text{SiO}_4$ component contribute to configurational entropy, is not warranted.

499 Instead, ordering of vacancies adjacent to the REE³⁺ cations that they charge-balance produces
 500 $(a_{\text{REE}_{4/3}\text{SiO}_4}^{\text{fo}})^{3/4} \propto c_{\text{REE}}^{\text{fo}}$, and Henry's Law is maintained (Appendix A). Both mechanisms are consistent
 501 with Henry's Law, which cannot be used to discriminate between them.

502

503 Colson et al. (1989), in their evaluation of experiments previously reported in Colson et al. (1988),
 504 also noted the possibility of both substitution mechanisms operating in combination in olivine, but
 505 concluded that “the larger cations in olivine (Sc, Yb) are charge-balanced primarily by (octahedral site
 506 vacancies)”. They did not attempt to quantify “primarily”, partly due to their precision being limited
 507 by their reliance on electron microprobe analyses at trace concentrations, but also because the
 508 experiments of Colson et al. (1988) encompass two additional variables: a large range of Mg/Fe in
 509 olivine, and temperatures varying from 1169 to 1414°C. Colson et al. (1989) contrasted their
 510 conclusion that the REE and Sc substituted in olivine charge-balanced by vacancies against their
 511 evidence that Sc substituted into what they called “low-Ca pyroxene” in their experiments by charge-
 512 balancing with tetrahedral Al. This “low-Ca pyroxene” is unlikely to be protoenstatite, at least in
 513 most of their experiments, because this phase is not stable at the low Mg/Fe of their compositions
 514 (see, for example, Ohi and Miyake 2016 and references therein).

515

516 *5.2 Implications for lattice strain models*

517 Lattice strain theory proposes that mineral/melt partition coefficients among a suite of cations of the
 518 same charge and with spherically symmetric electron configurations, such as the REEs, vary with
 519 their ionic radii. Several formulations of this concept have been proposed since the fundamentals of
 520 the idea were introduced by Mott and Littleton (1938), among which one due to Brice (1975) has
 521 come to dominate in the Earth sciences literature following the demonstration of its usefulness by
 522 Blundy and Wood (1994). Note, however, that Beattie (1994) applied a different formulation, after
 523 Nagasawa (1966), to fit his REE olivine/melt partitioning data. The Brice equation is:

$$\ln D_{\text{REE}} = \ln D_0 - \frac{4\pi EN_A}{RT} \left(\frac{r_0}{2} (r_{\text{REE}} - r_0)^2 + \frac{1}{3} (r_{\text{REE}} - r_0)^3 \right) \quad (15)$$

524 where D_0 is the partition coefficient for a hypothetical 3+ cation of ionic radius r_0 , E is the Young's
 525 modulus of the cation site, and N_A is Avogadro's number. Comparison with the thermodynamic
 526 formulation (e.g., Eqns. 11 or 12) shows that the second term on the right-hand side is equivalent to
 527 $\ln Y_{\text{REE}_{4/3}\text{SiO}_4}^{\text{fo}}$ or $\ln Y_{\text{REEMgAlO}_4}^{\text{fo}}$, respectively, which leaves D_0 to incorporate three quantities: the
 528 equilibrium constant (that is, a ΔG° term), $\gamma_{\text{REEO}_{1.5}}^{\text{melt}}$, and the stoichiometric control. The presumption
 529 has been that the three contributions to D_0 are not functions of the cation's identity (hence of r_{REE}),
 530 therefore the variation of $\ln D_{\text{REE}}$ with r_{REE} is entirely due to the lattice strain term, which has a very
 531 specific shape: that of a slightly asymmetric parabola.

532 As shown in Section 4.5 and Fig. 7, this cannot be correct in detail, because the sensitivity of $\gamma_{\text{REEO}_{1.5}}^{\text{melt}}$
 533 to melt composition depends on the REE, hence r_{REE} (Eqn. 14). Furthermore, if we apply Eqn. (15) to
 534 each of the two substitution mechanisms in forsterite (Fig. 6a), we find differences in their E and r_0 ,
 535 despite the probability that the REEs occupy the same crystallographic site in both substitution
 536 mechanisms. The curve for $D_{\text{REE}(\text{vac})}^{\text{fo/melt}}$ versus r_{REE} gives $E_{\text{vac}} = 415(19)$ GPa and $r_{0,\text{vac}} = 0.713(7)$ Å,
 537 while that for $D_{\text{REE}(\text{Al})}^{\text{fo/melt}}$ versus r_{REE} gives $E_{\text{Al}} = 625(28)$ GPa and $r_{0,\text{Al}} = 0.740(4)$ Å. An explanation is
 538 that $\Delta G^{\circ}_{(\text{fo}, \text{vac})}$ and $\Delta G^{\circ}_{(\text{fo}, \text{Al})}$ are, firstly, functions of r_{REE} , and, secondly, different functions of r_{REE} .
 539 There is no theoretical reason that such quantities as $\Delta G^{\circ}_{(\text{fo}, \text{vac})}$ and $\Delta G^{\circ}_{(\text{fo}, \text{Al})}$ would vary with r_{REE}
 540 according to the same slightly asymmetric parabolic shape as that deduced by Brice (1975) for lattice
 541 strain in Eq. (15). Of the three thermodynamic factors listed above as contributing to D_0 , only one, the
 542 stoichiometric control, is expected not to vary with r_{REE} .

543
 544 A literal interpretation of the lattice strain models of Nagasawa (1966) or Brice (1975) also encounters
 545 the problematic nature of the concept of ionic radii. Ionic radii could in principle be derived from
 546 interatomic distances in crystals by splitting up that part of the electron density associated with the
 547 cation from that associated with the anion (e.g., Gibbs et al. 2013). In practice the splitting-up is not
 548 done, and instead a fictive radius is assigned to the anion (here, O^{2-}) and the cation's radius is then
 549 found by subtracting the anion's fictive radius from the interatomic distance (Shannon, 1976). So by
 550 "ionic radius" what is really meant is interatomic distance. Except in geometrically simple, high-
 551 symmetry crystal structures like halite, the interatomic distances defining a coordination polyhedron
 552 often vary considerably. The M2 site in forsterite, which is probably the site that hosts the REE, like
 553 in (Li,Na)REESiO₄ olivine (Blasse and Bril 1967) and is the site occupied by similarly sized Ca^{2+} in
 554 CaMgSiO₄, e.g., Lumpkin and Ribbe 1983) has been identified as an egregious example of a site
 555 whose distortion from regular geometry is so profound that it is difficult to parameterize (Dollase
 556 1974). The second problem is specific to the radii of the REE in six-fold coordination ($r_{\text{REE}}^{\text{VI}}$), which
 557 Eq.(15) would seem to require to best match the relevant cation sites in both forsterite and
 558 protoenstatite. The values of $D_{\text{REE}}^{\text{fo/melt}}$ and $D_{\text{REE}}^{\text{prEn/melt}}$ are smooth functions of atomic number (Z), as are
 559 the more widely used radii in eight-fold coordination from Shannon (1976) to 0.001 \AA ($r_{\text{REE}}^{\text{VIII}}$), but
 560 $r_{\text{REE}}^{\text{VI}}$, from the same source are not. We take this to be a deficiency in the latter, since there is no
 561 conceivable physical explanation for such a difference. The values from Shannon (1976) are
 562 essentially those of Shannon and Prewitt (1970) except for La and Pr. The revision to Pr appears
 563 anomalous; it may be a typographical error (0.99 for 0.997). Part of the difficulty is that crystal data
 564 for the light REE in 6-fold coordination are relatively few. Evans et al. (2008) noticed the lack of
 565 smoothness in the values of $r_{\text{REE}}^{\text{VI}}$, and allowed their values to vary in their regressions of $D_{\text{REE}}^{\text{fo/melt}}$ vs.
 566 $r_{\text{REE}}^{\text{VI}}$, but in so far as their refined values still do not eliminate the lack of smoothness, that approach
 567 may have been too conservative.

568

569 In summary, the Brice equation and similar equations (e.g., Nagasawa 1966) that actualize the
570 concept of ionic radii are only approximations. For REE mineral/melt partition coefficients, the Brice
571 equation has been useful in identifying aberrant data, and interpolating between measured D_{REE} to
572 obtain partition coefficients for REE that were not measured. Whether it has predictive power is more
573 contentious. For example, Evans et al. (2008) noted that fitting $D_{\text{REE}}^{\text{fo/melt}}$ to the lattice strain model did
574 not predict $D_{\text{Sc}}^{\text{fo/melt}}$ well, which they ascribed to Sc substituting in both the M1 and M2 sites, whereas
575 the REEs may substitute only into M2 (like Ca). Our present results add other possibilities to account
576 for this predictive failure.

577

578 Despite the dubious theoretical justification for the Brice equation, Sun and Liang (2013) assumed its
579 validity as the starting point for their parameterization of some experimental determinations of REE
580 olivine/melt partition coefficients. A comparison between $D_{\text{REE}}^{\text{fo/melt}}$ measured in the present study and
581 the predictions from the parameterization of Sun and Liang (2013) is presented in Fig. 10. Most
582 partition coefficients are reproduced to within $\pm 30\%$, but there are systematic offsets caused by the
583 flaws in their approach. With increasing $X_{\text{AlO}_{1.5}}^{\text{melt}}$ the mismatch for the heavy REE and Sc increases,
584 because their parameterization does not account for the competing effects of $X_{\text{AlO}_{1.5}}^{\text{melt}}$ and $a_{\text{SiO}_2}^{\text{melt}}$, using
585 only $X_{\text{AlO}_{1.5}}^{\text{melt}}$ as a variable. Moreover, with increasing $X_{\text{AlO}_{1.5}}^{\text{melt}}$ the mismatch with our data develops a
586 dependence on ionic radius for the heavy REE and Sc because their model assumes a constant E
587 parameter for forsterite, in contrast to our observation of a narrower parabola for the REEMgAlO₄
588 substitution.

589

590 Parameterizing mineral/melt partition coefficients of the REEs as a function of their ionic radii is
591 useful for petrological modelling (e.g., O'Neill 2016). Insofar as such parameterizations aim to fit the
592 data as faithfully as possible, there is no compelling need to force them into the form of the Brice
593 equation, or other models that have limited theoretical validity. To emphasise this point, we show that
594 an empirical parameterization that is more faithful to the experimental results may be obtained by
595 avoiding the Brice equation, simply by fitting values of $D_{\text{REE}}^{\text{fo/melt}}$ to polynomials in $r_{\text{REE}}^{\text{VIII}}$. We use $r_{\text{REE}}^{\text{VIII}}$
596 rather than $r_{\text{REE}}^{\text{VI}}$ in deference to the deficiency in physical reality that the concept of ionic radii has for
597 distorted coordination polyhedra like the M2 site of olivine, and the uncertainty surrounding
598 Shannon's values for $r_{\text{REE}}^{\text{VI}}$. Each set of $D_{\text{REE}}^{\text{fo/melt}}$ values from Evans et al. (2008) and this study (14 sets)
599 was fitted to the orthogonal polynomials of O'Neill (2016):

600
$$\ln D_{\text{REE}}^{\text{fo/melt}} = \sum_n \delta_n f_{\text{orth}}^n \quad (16a)$$

601 The advantage of the orthogonal polynomials lies with each term being independent of the others.
602 Hence each term can be fitted to an expression for melt composition, using the insights gained from
603 this study:

$$604 \quad \delta_n = a_0 + a_{Si}(X_{SiO_2}^{melt} - 0.52) + a_{Al}X_{AlO_{1.5}}^{melt} + a_{Ca}X_{CaO}^{melt} + a_{Ti}X_{TiO_2}^{melt} \quad (16b)$$

605 The results of this fit with the orthogonal polynomial truncated at $n = 2$ is shown for comparison with
606 the Sun and Liang model in Fig. 10. Even with only a second order polynomial, much of the
607 systematic error caused by applying the Brice equation is eliminated. Adding in the next term in the
608 orthogonal polynomial ($n = 3$) improves the fit further, but is not warranted given the precision of the
609 data.

610

611 The requirements of any parameterization centre around the need to represent data to within their
612 uncertainties as exactly as possible. Because the lattice strain theory due to Brice (1975) is based on
613 simplifying assumptions that cannot be true in detail, it is unrealistic to expect that it would fulfil such
614 an obligation. As shown for the example of REE olivine/melt partition coefficients here, it may
615 generally be expected that better representations of partition data can be achieved without imposing
616 the constraints inherent in the Brice equation. Against the empirical approach is the loss of predictive
617 power for other trivalent cations (e.g., Sc), which can be resolved by using both approaches according
618 to context.

619

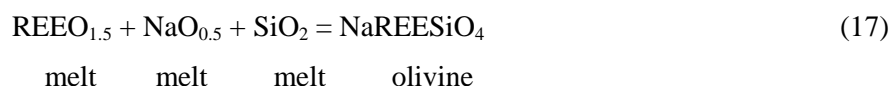
620 **6. Conclusions**

621 The aim of the present study is to demonstrate a general principle that needs to be explicitly
622 acknowledged in parameterizations of trace-element partition coefficients, namely that multiple
623 substitution mechanisms for the same element in the same mineral may occur. Substitution of the
624 REE³⁺ into both forsterite and protoenstatite by a combination of vacancy- and Al-balanced
625 mechanisms are examples of a phenomenon that is likely important elsewhere in trace-element
626 geochemistry. For example, at least three charge balance mechanisms are known for REE in zircon
627 (Burnham and Berry, 2017). We suspect that the operation of multiple mechanisms is probably more
628 the rule than the exception in minerals of interest to igneous petrologists.

629

630 For olivine and probably also pyroxenes, additional mechanisms include those where REE³⁺ is
631 coupled with univalent cations ($2Mg^{2+} = M^+ + REE^{3+}$, where M^+ is H^+ , Li^+ or Na^+ , e.g. Purton et al.,
632 1997). The hydrous component, $REE_{\square}SiO_4(OH)$, has been demonstrated by Berry et al. (2007). The
633 orthosilicate $LiScSiO_4$ is a stable, olivine-structured endmember of this substitution type (Steele et al.
634 1978), but $LiREE^{3+}SiO_4$ components are unlikely to be a significant in natural basaltic systems, where
635 the low availability of Li is the limiting factor. Because of the much higher abundance of Na in

636 basalts, $\text{NaREE}^{3+}\text{SiO}_4$ may be more significant, albeit offset by the lower compatibility of Na in
 637 olivine. The reaction for this would be:



638 and the stoichiometric control indicates $D_{\text{REE}}^{\text{ol}/\text{melt}} \propto a_{\text{SiO}_2}^{\text{melt}}$. This putative substitution requires
 639 experimental investigation, as does the potential for Na-REE interactions to lead to changes in
 640 $\gamma_{\text{REEO}_{1.5}}^{\text{melt}}$ (Michely et al., 2017). For this reason it would be premature to attempt another
 641 parameterization of REE olivine/melt partitioning. Whether the substitution $2\text{Mg}^{2+} = \text{M}^+ + \text{R}^{3+}$ is
 642 significant in protoenstatite is unknown; it does not appear to matter in enstatite, at least with Li^+ as
 643 M^+ (van Kan Parker et al. 2011).

644
 645 Another conclusion from this study is that unless ways can be found to achieve a satisfactory isolation
 646 of variables, it will be difficult to infer substitution mechanisms from mineral/melt partition
 647 coefficients reliably. This difficulty may be anticipated to be greater in crystals with more complex
 648 stoichiometry and composition than forsterite (i.e., most rock-forming minerals), and independent
 649 evidence from spectroscopy and computational studies may be needed. In particular, the slopes of the
 650 correlation between mineral/melt partition coefficients and major-element oxide components cannot
 651 be used to infer substitution stoichiometries (cf. Lundstrom et al., 1994), because these depend on
 652 both the free energy of the partitioning reaction and the activity coefficient of the oxide species in the
 653 melt, as well as the stoichiometric control. For example, see Eqn. 14, which summarizes the reasons
 654 why the slopes of $D_{\text{REE}}^{\text{fo}/\text{melt}}$ versus $X_{\text{AlO}_{1.5}}^{\text{melt}}$ differ among the REEs (Fig. 5), despite the substitution
 655 mechanism being identical for all REE.

656
 657 Apart from the issues of multiple substitution mechanisms and their stoichiometric controls, this study
 658 also confirms the finding of Evans et al. (2008) that the activity coefficient of $\text{REEO}_{1.5}$ components in
 659 silicate melts vary as a function of melt composition, particularly silica content, and this variation
 660 differs systematically among the REE as a function of ionic radius. Here we also show that even at
 661 constant silica activity other aspects of melt composition can affect $\gamma_{\text{REEO}_{1.5}}^{\text{melt}}$ and hence partitioning,
 662 for example the REE-Ti interactions implied by the difference between D_{REE} in the base and high-Ti
 663 compositions. Note that factors affecting $\gamma_{\text{REEO}_{1.5}}^{\text{melt}}$ are common to all REE mineral/melt partition
 664 coefficients, and need to be included in any parameterization, whatever the mineral.

665
 666 **APPENDIX A. The relationship between concentration and activity for the REE in forsterite**

667 There are two separate issues: one is the relationship between concentration and mole fraction, which
 668 in the case of the crystalline phase is needed to evaluate site occupancies hence configurational
 669 entropies of mixing; the other is allowing for contributions to the activity that are additional to the

670 configurational entropy, through activity coefficients. For trace elements, concentrations are simply
671 proportional to mole fractions, and defining activity coefficients in terms of concentrations bypasses
672 the step of explicitly relating concentrations to mole fractions and site occupancies. Thus, in the
673 present example, the activity of the REE³⁺ component, $a_{\text{REE}_{4/3}\text{SiO}_4}^{\text{fo}}$ (Eq. 2), should depend on $c_{\text{REE}}^{\text{fo}}$
674 raised to some power that depends on the configurational entropy of mixing, that is, mixing of REE³⁺,
675 Mg²⁺ and the vacancies on the octahedral sites of forsterite. The experimental observation is that
676 $D_{\text{REE}}^{\text{fo/melt}}$ is constant over a substantial range of concentrations (Henry's law), implying that
677 $(a_{\text{REE}_{4/3}\text{SiO}_4}^{\text{fo}})^{3/4} = c_{\text{REE}}^{\text{fo}} \gamma_{\text{REE}_{4/3}\text{SiO}_4}^{\text{fo}}$, while $a_{\text{REEO}_{1.5}}^{\text{melt}} = c_{\text{REE}}^{\text{melt}} \gamma_{\text{REEO}_{1.5}}^{\text{melt}}$, where $\gamma_{\text{REE}_{4/3}\text{SiO}_4}^{\text{fo}}$ and $\gamma_{\text{REEO}_{1.5}}^{\text{melt}}$ are the
678 activity coefficients defined in terms of concentration with respect to the standard state of infinite
679 dilution. Substituting these relations into Eq. 2 and rearranging gives:

$$D_{\text{REE}}^{\text{fo/melt}} = K_{(\text{fo}, \text{vac})} (\gamma_{\text{REEO}_{1.5}}^{\text{melt}} / \gamma_{\text{REE}_{4/3}\text{SiO}_4}^{\text{fo}}) (a_{\text{SiO}_2}^{\text{melt}})^{3/4}$$

$$= \exp\{-\Delta G_{(\text{fo}, \text{vac})}^{\circ} / RT\} (\gamma_{\text{REEO}_{1.5}}^{\text{melt}} / \gamma_{\text{REE}_{4/3}\text{SiO}_4}^{\text{fo}}) (a_{\text{SiO}_2}^{\text{melt}})^{3/4}$$

680
681
682 Similarly, without experiment or the equivalent atomistic calculations, it is ambiguous how
683 $a_{\text{REEMgAlO}_4}^{\text{fo}}$ (Eq. 5) relates to the concentration of Al in the forsterite, $c_{\text{Al}}^{\text{fo}}$. One conceptual possibility
684 is that the configurational entropy of the substitution comes from mixing of REE³⁺ with Mg²⁺ on the
685 octahedral sites happening independently of the mixing of Al³⁺ with Si⁴⁺ on the tetrahedral sites, in
686 which case $a_{\text{REEMgAlO}_4}^{\text{fo}} \propto (c_{\text{REE}}^{\text{fo}} c_{\text{Al}^{[4]}}^{\text{fo}})$. But experimental evidence indicates a high degree of short-
687 range order between octahedral and tetrahedral Al in forsterite (Evans et al., 2008; Burnham and
688 O'Neill, 2016), suggesting that the charge-balancing of REE³⁺ by tetrahedral Al is also short-range
689 ordered, and hence $a_{\text{REEMgAlO}_4}^{\text{fo}} \propto c_{\text{REE}}^{\text{fo}}$ is more likely. With this latter mechanism:

$$D_{\text{REE}}^{\text{fo/melt}} = K_{(\text{fo}, \text{Al})} (\gamma_{\text{REEO}_{1.5}}^{\text{melt}} / \gamma_{\text{REEMgAlO}_4}^{\text{fo}}) a_{\text{AlO}_{1.5}}^{\text{melt}} (a_{\text{SiO}_2}^{\text{melt}})^{-1/2}$$

$$= \exp\{-\Delta G_{(\text{fo}, \text{Al})}^{\circ} / RT\} (\gamma_{\text{REEO}_{1.5}}^{\text{melt}} / \gamma_{\text{REEMgAlO}_4}^{\text{fo}}) a_{\text{AlO}_{1.5}}^{\text{melt}} (a_{\text{SiO}_2}^{\text{melt}})^{-1/2}$$

690
691 **APPENDIX B. Calculation of $\gamma_{\text{REEO}_{1.5}}^{\text{melt}}$ for the data of Evans et al. (2008)**

692 Values of $D_{\text{REE}(\text{vac})}^{\text{fo/melt}}$ may be related to those on the fo+prEn cotectic ($D_{\text{REE}(\text{vac})}^{\text{fo/melt}, \text{f+p}}$) at the same
693 temperature (≈ 1400 °C) and pressure (1 bar) by:

$$D_{\text{REE}(\text{vac})}^{\text{fo/melt}} = D_{\text{REE}(\text{vac})}^{\text{fo/melt}, \text{f+p}} (\gamma_{\text{REEO}_{1.5}}^{\text{melt}} / \gamma_{\text{REEO}_{1.5}}^{\text{melt}, \text{f+p}}) (a_{\text{SiO}_2}^{\text{melt}} / a_{\text{SiO}_2}^{\text{melt}, \text{f+p}})^{3/4} \quad (\text{B.1})$$

694

695 To apply this relationship to the results of Evans et al. (2008), we make the enabling assumption that
 696 $\gamma_{\text{SiO}_2}^{\text{melt}}$ remains constant (as it did on the forsterite-protoenstatite cotectic), such that $a_{\text{SiO}_2}^{\text{melt}}/a_{\text{SiO}_2}^{\text{melt, f+p}} \approx$
 697 $X_{\text{SiO}_2}^{\text{melt}}/X_{\text{SiO}_2}^{\text{melt, f+p}}$. Hence:

$$D_{\text{REE(vac)}}^{\text{fo/melt}} \approx D_{\text{REE(vac)}}^{\text{fo/melt, f+p}} (\gamma_{\text{REEO}_{1.5}}^{\text{melt}}/\gamma_{\text{REEO}_{1.5}}^{\text{melt, f+p}}) (X_{\text{SiO}_2}^{\text{melt}}/X_{\text{SiO}_2}^{\text{melt, f+p}})^{3/4} \quad (\text{B.2})$$

698

699 For the Al-substitution mechanism, we also need to make the analogous enabling assumption that
 700 $\gamma_{\text{AlO}_{1.5}}^{\text{melt}}$ is constant. This allows us to work in terms of $X_{\text{AlO}_{1.5}}^{\text{melt}}$:

$$D_{\text{REE(Al)}}^{\text{fo/melt}} \approx \frac{dD_{\text{REE(Al)}}^{\text{fo/melt, f+p}}}{dX_{\text{AlO}_{1.5}}^{\text{melt}}} X_{\text{AlO}_{1.5}}^{\text{melt}} (\gamma_{\text{REEO}_{1.5}}^{\text{melt}}/\gamma_{\text{REEO}_{1.5}}^{\text{melt, f+p}}) (X_{\text{SiO}_2}^{\text{melt}}/X_{\text{SiO}_2}^{\text{melt, f+p}})^{-1/2} \quad (\text{B.3})$$

701

702 Summing $D_{\text{REE(vac)}}^{\text{fo/melt}}$ and $D_{\text{REE(Al)}}^{\text{fo/melt}}$, and rearranging, gives:

$$\begin{aligned} \gamma_{\text{REEO}_{1.5}}^{\text{melt}}/\gamma_{\text{REEO}_{1.5}}^{\text{melt, f+p}} \approx & D_{\text{REE}}^{\text{fo/melt}} / [D_{\text{REE(vac)}}^{\text{fo/melt, f+p}} (X_{\text{SiO}_2}^{\text{melt}}/X_{\text{SiO}_2}^{\text{melt, f+p}})^{3/4} \\ & + \frac{dD_{\text{REE(Al)}}^{\text{fo/melt, f+p}}}{dX_{\text{AlO}_{1.5}}^{\text{melt}}} \frac{dD_{\text{REE(Al)}}^{\text{fo/melt, f+p}}}{dX_{\text{AlO}_{1.5}}^{\text{melt}}} X_{\text{AlO}_{1.5}}^{\text{melt}} (X_{\text{SiO}_2}^{\text{melt}}/X_{\text{SiO}_2}^{\text{melt, f+p}})^{-1/2}] \end{aligned} \quad (\text{B.4})$$

703

704 where $X_{\text{SiO}_2}^{\text{melt, f+p}}$ is taken as 0.52.

705

706 Figure Captions

707 Fig. 1 Comparison of protoenstatite/melt and forsterite/melt partition coefficients from the base
 708 composition (solid symbols) except where elements were below the detection limit in forsterite: Ti
 709 (values from the high-Ti composition), Al (values are averages of the low- and high-Al compositions,
 710 with the range shown by the error bar) and Na (protoenstatite D_{Na} is an average of all other
 711 compositions; forsterite D_{Na} is from composition AB011 of Burnham and O'Neill, 2016). The 1:1 line
 712 is shown for reference.

713 Fig. 2 A comparison of protoenstatite/melt partition coefficients for the REE and Y in the base and
 714 high-Ti compositions, showing La, Ce, Pr and Nd deviating from a linear correlation between the two
 715 datasets, inferred to be due to melt contamination (see text for discussion). Errors are 1σ of replicate
 716 analyses.

717 Fig. 3 Dependence of D_{Ca} on X_{CaO} of the melt for protoenstatite (solid symbols) and forsterite (open
 718 symbols). Errors are 1σ of replicate analyses.

719 Fig. 4 Comparison of $c_{\text{REE}}^{\text{melt}}$ and $D_{\text{REE}}^{\text{fo/melt}}$ of the high-Al composition of this study with experiment
 720 MMC-2 of Di Stefano et al. (2018). The concentrations of the REE vary by over four orders of
 721 magnitude between the two experiments but this variation results in negligible deviation from a 1:1
 722 correlation (dashed line), attesting to the validity of Henry's Law.

723 Fig. 5 Dependence of forsterite/melt partition coefficients on $X_{\text{AlO}_{1.5}}^{\text{melt}}$ with the linear best fits to the
724 data. Y and Ho have a consistent relationship to each other despite a factor of 150 difference in
725 doping concentrations, suggesting little deviation from Henry's Law. Errors are 1σ of replicate
726 analyses; the data for Y in panel (c) are offset to slightly higher $X_{\text{AlO}_{1.5}}^{\text{melt}}$ for clarity.

727 Fig. 6 Mineral/melt partition coefficients for a) forsterite, and b) protoenstatite, split into the
728 separate contributions from the vacancy and Al-coupled mechanisms. The latter are calculated at
729 $X_{\text{AlO}_{1.5}}^{\text{melt}} = 0.15$, a typical value for basaltic liquids. The curves are the fits to Eq. 15.

730 Fig. 7 Calculated $\gamma_{\text{MO}_{1.5}}^{\text{melt}}/\gamma_{\text{MO}_{1.5}}^{\text{melt, f+p}}$ as a function of $X_{\text{SiO}_2}^{\text{melt}}$ in CMAS compositions at $\sim 1400^\circ\text{C}$ from
731 Evans et al. (2008) and this study, showing the greater sensitivity to melt composition of the light
732 REE (here exemplified by La) compared to the heavy REE (Lu) and Sc.

733 Fig. 8 Dependence of protoenstatite/melt partition coefficients on $X_{\text{AlO}_{1.5}}^{\text{melt}}$ and the linear best fits to
734 the data; unlike for forsterite/melt the dependence on $X_{\text{AlO}_{1.5}}^{\text{melt}}$ is approximately the same for all
735 trivalent cations.

736 Fig. 9 Dependence of $D_{\text{Zr}}^{\text{fo/melt}}$ on $X_{\text{AlO}_{1.5}}^{\text{melt}}$ for the present study (solid symbols) and Evans et al.
737 (2008). The rate of variation is greater for Zr than a REE of similar incompatibility.

738 Fig. 10 The ratios of D_{REE} predicted using the model of Sun and Liang (2013) to the results of the
739 present study, as a function of ionic radius (solid circles), for a) the base composition, b) the low-Al
740 composition, c) the high-Al composition and d) the high-Ti composition. For comparison, the fit to an
741 empirical equation (Eqn. 16 in the text) is also shown (open circles).

742

743 **References**

- 744 Beattie P (1994) Systematics and energetics of trace-element partitioning between olivine and silicate
745 melts: Implications for the nature of mineral/melt partitioning. *Chem Geol* 117: 57-71.
- 746 Berry AJ, O'Neill HStC, Hermann J (2007) The infrared signature of water associated with trivalent
747 cations in olivine. *Earth Planet Sci Lett* 261: 134-142.
- 748 Blasse, G., & Brill, A. (1967). Structure and Eu^{3+} -fluorescence of lithium and sodium lanthanide
749 silicates and germanates. *Journal of Inorganic and Nuclear Chemistry*, 29, 2231-2241.
- 750 Blundy JD, Wood BJ (1994) Prediction of crystal-melt partition coefficients from elastic moduli.
751 *Nature* 372: 452-454.
- 752 Boström D (1989) Cation ordering at 1300°C in the (Ni, Mg)-olivine solid-solution series. *Acta Chem*
753 *Scand* 43:116–120
- 754 Brice JC (1975) Some thermodynamics aspects of the growth of strained crystals. *J Crystal Growth*
755 28: 249-253.
- 756 Burnham AD, Berry AJ (2014) The effect of oxygen fugacity, melt composition, temperature and
757 pressure on the oxidation state of Ce in silicate melts. *Chem Geol* 366, 52-60.

758 Burnham AD, Berry AJ (2017) Formation of Hadean granites by melting of igneous crust. *Nature*
759 *Geosci* 10: 457-461

760 Burnham AD, Berry AJ, Halse HR, Schofield PF, Cibin G, Mosselmans JFW (2015) The oxidation
761 state of Eu in silicate melts as a function of oxygen fugacity, composition and temperature. *Chem*
762 *Geol* 411: 248-259

763 Burnham AD, O'Neill HStC (2016) The effect of melt composition on mineral-melt partition
764 coefficients: The case of beryllium. *Chem Geol* 442: 139-147.

765 Callen HB (1985) *Thermodynamics and an Introduction to Thermostatistics*. 2nd Edition, John Wiley
766 & Sons, Hoboken, NJ.

767 Colson RO, McKay GA, Taylor LA (1988) Temperature and composition dependencies of trace
768 element partitioning: Olivine/melt and low-Ca pyroxene/melt. *Geochim Cosmochim Acta*: 52, 539-
769 553.

770 Colson RO, McKay GA, Taylor LA (1989). Charge balancing of trivalent trace elements in olivine
771 and low-Ca pyroxene: A test using experimental partitioning data. *Geochim Cosmochim Acta* 53:
772 643-648.

773 Di Stefano F, Mollo S, Scarlato P, Nazzari M, Bachmann O, Caruso, M (2018) Olivine compositional
774 changes in primitive magmatic skarn environments: A reassessment of divalent cation partitioning
775 models to quantify the effect of carbonate assimilation. *Lithos* 316: 104-121

776 Dollase WA (1974) A method of determining the distortion of coordination polyhedra. *Acta*
777 *Crystallogr A*30: 513-517.

778 Duffy JA (2005) Polarisability and polarising power of rare earth ions in glass: an optical basicity
779 assessment. *Phys Chem Glasses* 46: 1-6.

780 Evans TM, O'Neill HStC Tuff J (2008) The influence of melt composition on the partitioning of
781 REEs, Y, Sc, Zr and Al between forsterite and melt in the system CMAS. *Geochim Cosmochim*
782 *Acta* 72: 5708-5721.

783 Gibbs GV, Ross NL, Cox DF, Rosso KM, Iversen BB Spackman MA (2013) Bonded radii and the
784 contraction of the electron density of the oxygen atom by bonded interactions. *J Phys Chem A* 117:
785 1632-1640.

786 Grant KJ, Wood BJ (2010) Experimental study of the incorporation of Li, Sc, Al and other
787 trace elements into olivine. *Geochim Cosmochim Acta* 74: 2412–2428.

788 Jarosewich E, Boatner LA (1991) Rare-earth element reference samples for electron microprobe
789 analysis. *Geostandards Newsletter* 15, 397-399.

790 Jenner FE, O'Neill HStC (2012) Major and trace analysis of basaltic glasses by laser-ablation ICP-
791 MS. *Geochem, Geophys, Geosystems*, 13: Q03003.

792 Jochum KP, Weis U, Stoll B, Kuzmin D, Yang Q, Raczek I, Jacob DE, Stracke A, Birbaum K, Frick
793 DA, Günther D (2011) Determination of reference values for NIST SRM 610–617 glasses following
794 ISO guidelines. *Geostand Geoanal Res* 35: 397-429.

795 Jollands MC, O'Neill HStC, Hermann J (2014) The importance of defining chemical potentials,
796 substitution mechanisms and solubility in trace element diffusion studies: the case of Zr and Hf in
797 olivine. *Contrib Mineral Petrol* **168**: 1055.

798 Kamenetsky VS, Elburg M, Arculus R, Thomas R (2006) Magmatic origin of low-Ca olivine in
799 subduction-related magmas: co-existence of contrasting magmas. *Chem Geol* 233: 346-357.

800 Kogiso T, Tatsumi Y, Shimoda G, Barszczus HG (1997) HIMU ocean island basalts in southern
801 Polynesia; new evidence for whole mantle scale recycling of subducted oceanic crust. *J Geophys*
802 *Res B* 102: 8085–8103.

803 Kushiro I (1975) On the nature of silicate melt and its significance in magma genesis; regularities in
804 the shift of the liquidus boundaries involving olivine, pyroxene, and silica minerals. *Am J Sci* 275:
805 411-431.

806 Leitzke FP, Fonseca RO, Michely LT, Sprung P, Münker C, Heuser A, Blanchard H (2016) The effect
807 of titanium on the partitioning behavior of high-field strength elements between silicates, oxides and
808 lunar basaltic melts with applications to the origin of mare basalts. *Chem Geol* 440: 219-238.

809 Leitzke FP, Fonseca ROC, Sprung P, Mallmann G, Lagos M, Michely LT, Münker C (2017) Redox
810 dependent behaviour of molybdenum during magmatic processes in the terrestrial and lunar mantle:
811 Implications for the Mo/W of the bulk silicate Moon. *Earth Planet Sci Lett* 474: 503-515.

812 Longerich HP, Jackson SE, Günther D, (1996) Inter-laboratory note. Laser ablation inductively
813 coupled plasma mass spectrometric transient signal data acquisition and analyte concentration
814 calculation. *J Anal Atomic Spectr* 11: 899-904.

815 Longhi J, Walker D, Hays J F (1978) The distribution of Fe and Mg between olivine and lunar
816 basaltic liquids. *Geochim Cosmochim Acta* 42: 1545-1558.

817 Lumpkin GR, Ribbe PH (1983) Composition order–disorder and lattice parameters of olivines—
818 relationships in silicate, germanate, beryllate, phosphate and borate olivines. *Am Mineral* 68: 164-
819 176.

820 Lundstrom CC, Shaw HF, Ryerson FJ, Phinney DL, Gill JB, Williams Q (1994) Compositional
821 controls on the partitioning of U, Th, Ba, Pb, Sr and Zr between clinopyroxene and haplobasaltic
822 melts: implications for uranium series disequilibria in basalts. *Earth Planet Sci Lett* 128: 407-423.

823 McKay GA (1986) Crystal/liquid partitioning of the REE in basaltic systems: extreme fractionation of
824 the REE in olivine. *Geochim Cosmochim Acta* 50: 69-79.

825 Michely LT, Leitzke FP, Speelmans IM, Fonseca ROC (2017) Competing effects of crystal chemistry
826 and silicate melt composition on trace element behavior in magmatic systems: insights from
827 crystal/silicate melt partitioning of the REE, HFSE, Sn, In, Ga, Ba, Pt and Rh. *Contrib Mineral*
828 *Petrol* **172**: 39.

829 Mott NF, Littleton MJ (1938) Conduction in polar crystals. I. Electrolytic conduction in solid salts.
830 *Trans Faraday Soc* **34**: 485–499.

831 Nagasawa, H., 1966. Trace element partition coefficient in ionic crystals. *Science*, 152: 767-769.

832 Nernst W (1890) Über die Verteilung eines Stoffes zwischen zwei Lösungsmitteln. Nachr K Ges Wiss
833 Göttingen 12: 401-416.

834 Nernst W (1891) Verteilung eines Stoffes zwischen zwei Lösungsmitteln und zwischen Lösungsmittel
835 und Dampfraum. Z Phys Chem 8: 110-139.

836 Nielsen RL, Gallahan WE, Newburger F (1992) Experimentally determined mineral-melt partition
837 coefficients for Sc, Y and REE for olivine, orthopyroxene, pigeonite, magnetite and ilmenite.
838 Contrib Mineral Petrol 110: 488-499.

839 O'Neill H. StC (2016). The smoothness and shapes of chondrite-normalized rare earth element
840 patterns in basalts. J Petrol, 57: 1463-1508.

841 O'Neill HStC, Eggins SM (2002) The effect of melt composition on trace element partitioning: an
842 experimental investigation of the activity coefficients of FeO, NiO, CoO, MoO₂ and MoO₃ in
843 silicate melts. Chem Geol 186: 151-181.

844 Pack A, Russell SS, Shelley MG, van Zuilen M (2007) Geo- and cosmochemistry of the twin
845 elements yttrium and holmium. Geochim Cosmochim Acta 71: 4592-4608.

846 Purton JA, Allan NL, Blundy JD (1997). Calculated solution energies of heterovalent cations in
847 forsterite and diopside: implications for trace element partitioning. Geochim Cosmochim Acta 61:
848 3927-3936.

849 Putirka K (1999) Melting depths and mantle heterogeneity beneath Hawaii and the East Pacific Rise:
850 Constraints from Na/Ti and rare earth element ratios. J Geophys Res 104: 2817-2829.

851 Schoneveld L, O'Neill HStC (2019) The influence of melt composition on the partitioning of trace
852 elements between anorthite and silicate melt. Contrib Mineral Petrol: 174: 13

853 Seifert S, O'Neill HStC (1987) Experimental determination of activity-composition relations in
854 Ni₂SiO₄-Mg₂SiO₄ and Co₂SiO₄-Mg₂SiO₄ olivine solid solutions at 1200 K and 0.1 MPa and 1573 K
855 and 0.5 GPa. Geochim Cosmochim Acta 51: 97-104.

856 Shannon RD (1976) Revised effective ionic radii and systematic studies of interatomic distances in
857 halides and chalcogenides. Acta Crystall A 32: 751-767.

858 Shannon RD, Prewitt CT (1970) Revised values of effective ionic radii. Acta Crystall B 26: 1046-
859 1048.

860 Shaw DM (2006) Trace Elements in Magmas A Theoretical Treatment. Cambridge, UK.

861 Stead CV, Tomlinson EL, McKenna CA, Kamber BS (2017) Rare earth element partitioning and
862 subsolidus exchange behaviour in olivine. Chem Geol 475: 1-13.

863 Steele IM, Pluth JJ, Ito J (1978) Crystal structure of synthetic LiScSiO₄ olivine and comparison with
864 isotypic Mg₂SiO₄. Zeits Kristall Crystall Mat 147: 119-128.

865 Sun C, Liang Y (2013) The importance of crystal chemistry on REE partitioning between mantle
866 minerals (garnet, clinopyroxene, orthopyroxene, and olivine) and basaltic melts. Chem Geol 358:
867 23-36.

868 Takahashi E, Irvine TN (1981) Stoichiometric control of crystal/ liquid single-component partition
869 coefficients. *Geochim Cosmochim Acta* 45: 1181–1185.

870 Taura, H., Yurimoto, H., Kurita, K., & Sueno, S. (1998). Pressure dependence on partition
871 coefficients for trace elements between olivine and the coexisting melts. *Physics and Chemistry of*
872 *Minerals*, 25(7), 469-484.

873 van Kan Parker M, Mason PRD, van Westrenen W (2011) Experimental study of trace element
874 partitioning between lunar orthopyroxene and anhydrous silicate melt: Effects of lithium and iron.
875 *Chem Geol* 285: 1-14.

876 Yurimoto H, Sueno S (1987) Anion and cation partitioning between three pyroxenes, chrome spinel
877 phenocrysts and the host boninite magma: an ion microprobe study. *Geochem J* 21: 85-104.

878 Zhang F, Wright K (2010) Coupled (H^+ , M^{3+}) substitutions in forsterite. *Geochim Cosmochim Acta*
879 74: 5958-5965.

880 Zhukova I, O'Neill HStC, Campbell IH (2017) A subsidiary fast-diffusing substitution mechanism of
881 Al in forsterite investigated using diffusion experiments under controlled thermodynamic
882 conditions. *Contrib Mineral Petrol* 172: 53.

883 Zou H (2007) *Quantitative Geochemistry*. Imperial College Press, London.